*Composite Interfaces*, Vol 4, pp. 241–267 (1996)

Author prepared preprint

# On the use of energy methods for interpretation of results of single-fiber fragmentation experiments

JOHN A. NAIRN & YUNG CHING LIU
*Material Science and Engineering, University of Utah, Salt Lake City, Utah 84112, USA*

Received 5 May 1996; accepted 28 October, 1996

**Abstract**—We consider fragmentation experiments as a set of experimental results for fiber break density as a function of applied strain. This paper explores the potential for using fracture mechanics or energy methods in interpreting fragmentation experiments. We found that energy does not control fiber fracture; instead, fiber fracture releases much more energy than required to fracture the fiber. The excess released energy can lead to other damage mechanisms such as interfacial debonding. By assuming that all the excess released energy causes interfacial debonding and balancing energy using the energy release rate for debonding, we were able to determine interfacial toughness from fragmentation experiments. A reliable determination of interfacial toughness requires prior knowledge of interphase stress-transfer properties, fiber failure properties, actual damage mechanisms, and the coefficient of friction at the interface.

*Keywords:* fragmentation test; stress transfer; energy release rate; debonding; interface toughness

## 1. INTRODUCTION

In the single-fiber fragmentation test [1–6], a single fiber is embedded in a large amount of matrix and the specimen is loaded in tension until the fiber fragments. The loading is continued until the fragmentation process ceases. The results of a fragmentation experiment are data for the fiber break or crack density as a function of applied strain. The inverse of the saturation crack density is known as the critical fragment length. The goal of the fragmentation test has primarily been to learn about interfacial properties. It is difficult, however, to extract direct information about the interface from fragmentation results because the fragmentation process involves multiple failure processes and is influenced by many component mechanical properties. To learn about interfacial properties, we need to separate interface effects from the other effects that influence the experimental results.

The most obvious failure process in the fragmentation test is fiber fracture. This fracture is determined by fiber properties and has nothing to do with the interface. Once there are fiber breaks, however, the interface may begin to play a role. There are at least two interface properties that can influence the results. First, the interface plays a role in the ability of the matrix to transfer stress back into the broken fiber. Stress transfer needs to occur before more fiber fractures take place. Second, the interface itself may fail. A failed interface will further influence stress transfer and thus change the fragmentation process. Stress transfer and interfacial failure are distinct properties of the interface. For example, consider a composite system that has an interphase zone but has an infinitely strong interface. By influencing stress transfer, the interphase zone will influence the fragmentation results, but the fragmentation results give no information about interfacial failure because no failure is occurring. Real experiments will involve both stress transfer effects and interfacial failure effects. Their separate roles must be well understood before fragmentation results can be expected to give useful information about the interface.

This paper explores the use of fracture mechanics or energy methods for interpreting fragmentation experiments. To implement energy methods we first need to calculate the strain energy in a fiber fragment and the energy release rates for fiber fracture, interfacial debonding, or any other relevant failure mechanisms. We derived some exact linear elasticity results for energy. We were able to express the relevant strain energies

and energy release rates in terms of only the crack-opening displacement on the fiber, the interfacial shear stress, and the magnitude of any interfacial slip in the axial direction. These exact results were combined with a recent accurate stress analysis of the fragmentation test [7] to derive approximate expressions for the energy release rates due to fiber fracture and to interfacial debonding. Finally, these energy expressions and some strength models were used to predict fragmentation and fiber/matrix debonding experiments. The new models include both the stress transfer and failure properties of the interface. The stress transfer properties are included by using "interphase" parameters in the fragmentation stress analysis. The failure properties are included by predicting debonding using an interfacial toughness and fracture mechanics methods. The best models agree well with experimental results, but all models require further confirmation that the assumed failure mechanisms accurately represent the real failure mechanisms.

## 2. EXACT THEORETICAL RESULTS

We begin by describing some exact linear-elasticity results about the fragmentation specimen. The boundary conditions for finding the stresses and energy in a single fiber fragment in a fragmentation specimen are illustrated in Fig. 1. Region $R_1$ is an anisotropic fiber fragment. It has a circular cross section of radius $r_1$ and a length of $l$. Region $R_2$ is an infinite, isotropic matrix. The matrix extends from $r = r_1$ to $r = \infty$ and has a length $l$. The end conditions on the fiber and matrix are

$$\sigma_{zz,1}(r, z = \pm l/2) = \tau_{rz,1}(r, z = \pm l/2) = 0, \tag{1}$$

$$\tau_{rz,2}(r, z = \pm l/2) = 0, \tag{2}$$

$$W_2(r, z = \pm l/2) = \pm\frac{l}{2}\left(\frac{\sigma_0}{E_m} + \alpha_m T\right), \tag{3}$$

where subscripts "1" and "2" refer to the fiber and matrix, respectively. The fiber axial and shear stresses, $\sigma_{zz,1}$ and $\tau_{rz,1}$, are zero at the fragment ends because the fiber is fragmented and the ends are the fracture surface. The matrix shear stresses, $\tau_{rz,2}$, are zero and the matrix axial displacement, $W_2$, is constant or is independent of $r$. These matrix boundary conditions are required to maintain compatibility of the stress state in one fragment with that of the adjacent fragment in the specimen. The constant matrix displacement is determined by the net strain on the infinite matrix. For the uniaxial loading used in fragmentation tests, the net strain is simply calculated from the applied stress, $\sigma_0$, the temperature differential, $T = T_s - T_0$ where $T_s$ is the specimen temperature and $T_0$ is the stress-free temperature, and the modulus, $E_m$, and thermal expansion coefficient, $\alpha_m$, of the matrix.

During the fragmentation test, the interface may become damaged or may become partially or completely debonded. We therefore consider some additional conditions to describe the state of the interface. We introduce the square-bracket notation

$$[f] = f_2(r_1, z) - f_1(r_1, z), \tag{4}$$

to express the discontinuity in any function at the fiber/matrix interface. Regardless of the state of the interface, equilibrium dictates continuity in tractions or

$$[\sigma_{rr}] = [\tau_{rz}] = 0. \tag{5}$$

If the interface is intact and perfectly bonded, both the radial ($U$) and axial ($W$) displacements will also be continuous. The perfect interface conditions are

$$\text{Perfect Interface}: \quad [U] = [W] = 0. \tag{6}$$

Here we will generalize the intact interface to include intact, but imperfectly bonded interfaces. Hashin [8, 9] has proposed modeling imperfect interfaces in composites by allowing displacement discontinuities. He further proposed a simple linear relation between displacement discontinuities and the interfacial stress in the direction of the displacement. The Hashin imperfect interface conditions are

$$\text{Hashin Imperfect Interface}: \quad [U] = \frac{\sigma_{rr}(r_1, z)}{D_n} \quad \text{and} \quad [W] = \frac{\tau_{rz}(r_1, z)}{D_s}. \tag{7}$$

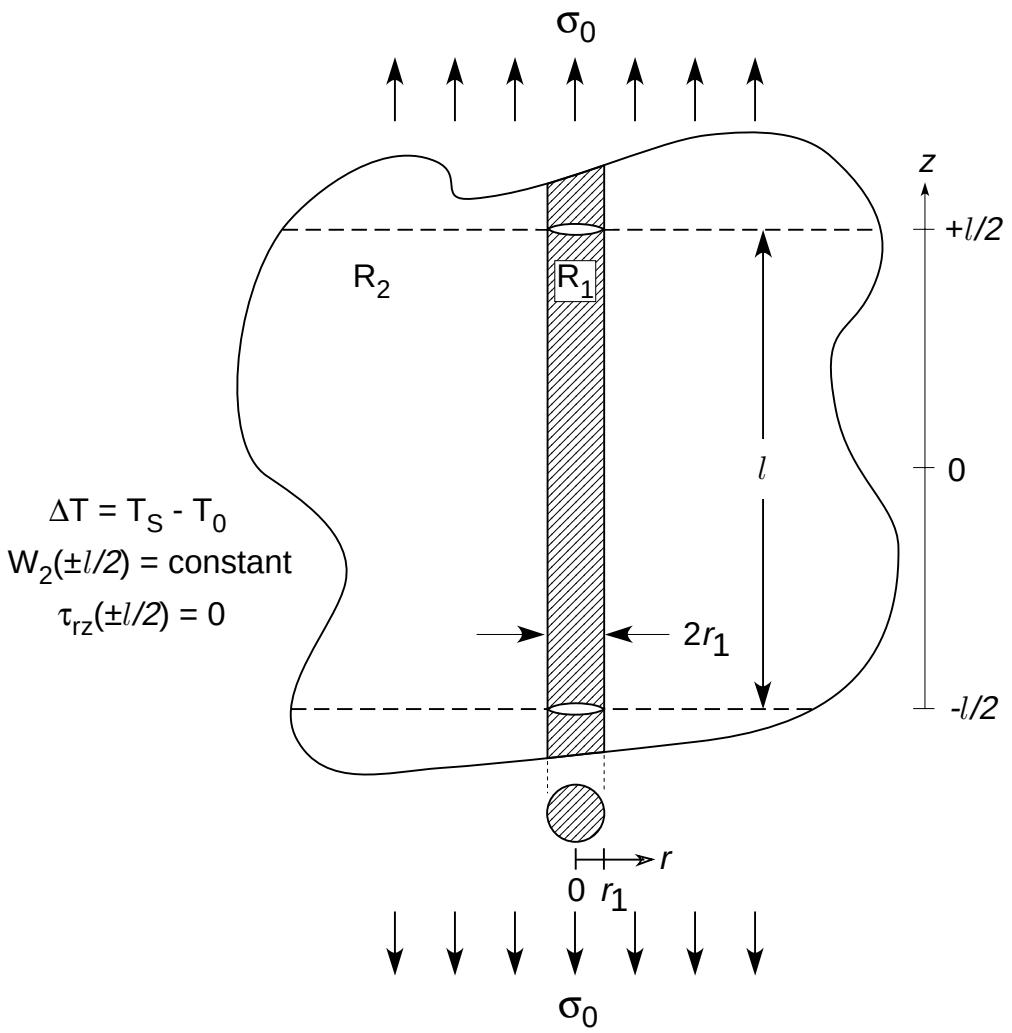


**Figure 1.** A cross section of a single fiber fragment of length $l$ and radius $r_1$ embedded in an infinite amount of matrix. The boundary conditions are indicated on the figure and described in the text of the paper (Note that $\sigma_0$ is the far-field matrix axial stress; the matrix axial stress at $\pm l/2$ is a function of $r$).

The constants $D_n$ and $D_s$ are known as interface parameters. $D_n = D_s = \infty$ corresponds to a perfect interface; $D_n = D_s = 0$ corresponds to a debonded interface; intermediate values of $D_n$ and $D_s$ correspond to an imperfect interface. In composites, $D_n$ and $D_s$ can viewed as modeling an interphase region between the fiber and the matrix [8, 9]. We will treat $D_s$ and $D_n$ as mechanical properties of the interface that describe its ability to transfer stress from the matrix to the fiber.

In the fragmentation test, both the tensile loading and the residual thermal stresses promote compressive radial stresses along the interface except for an extremely small zone near the fiber break [7]. Under dominantly compressive stress situations, $[U]$ should be zero to prevent penetration of the matrix into the fiber. Physically, a negative $[U]$ is allowed and it corresponds to compression of the interphase region. The capacity for this compression, however, is probably negligible. We claim an imperfect interface in the fragmentation test can thus be analyzed using

$$\text{Fragmentation Test Imperfect Interface}: \quad [U] = 0 \quad \text{and} \quad [W] = \frac{\tau_{rz}(r_1, z)}{D_s}. \tag{8}$$

There is thus a single interface parameter — $D_s$. We are not ignoring the possibility of an imperfect interface in the radial direction. We are simply exploiting the fact that the radial stresses in the fragmentation test

are mostly compressive, and, that as a result, an imperfect radial bond has little effect on fragmentation results.

Next, we consider a completely debonded interface. When the interface is debonded the displacement discontinuities are no longer related to the interfacial stresses and the interfacial stresses may be zero or nonzero depending on whether the debonded interface surfaces are separated or in contact. For a frictionless, debonded interface we have

$$\text{Frictionless Debonded Interface}: \begin{cases} [U] = \begin{cases} 0 & \text{if } \sigma_{rr}(r_1,z) < 0, \\ \geq 0 & \text{if } \sigma_{rr}(r_1,z) = 0, \end{cases} \\ [W] \neq 0, \\ \tau_{rz}(r_1,z) = 0. \end{cases} \tag{9}$$

If the debonded interface is in contact, the radial stress will be compressive ($\sigma_{rr}(r_1,z) < 0$) and $[U]$ must be zero. If the debonded interface is not in contact, the radial stresses will be zero and $[U]$ can be greater than zero as the crack opens. The debonded interface also has zero shear stresses and $[W]$ may be anything as the interface slips in the axial direction. For a debonded interface with friction we have

$$\text{Debonded Interface with Friction}: \begin{cases} [U] = \begin{cases} 0 & \text{if } \sigma_{rr}(r_1,z) < 0, \\ \geq 0 & \text{if } \sigma_{rr}(r_1,z) = 0, \end{cases} \\ [W] = \begin{cases} 0 & \text{if } \sigma_{rr}(r_1,z) < 0 \text{ and } \tau(r_1,z) < \mu\sigma_{rr}(r_1,z), \\ \neq 0 & \text{otherwise}, \end{cases} \\ \tau_{rz}(r_1,z) = \begin{cases} \mu\sigma_{rr}(r_1,z) & \text{if in frictional slip zone}, \\ \leq \mu\sigma_{rr}(r_1,z) & \text{otherwise}. \end{cases} \end{cases} \tag{10}$$

Regions where the debond surfaces are not in contact ($\sigma_{rr}(r_1,z) = 0$) are identical to the frictionless debond. Regions where there is contact are further subdivided into regions of frictional slip and regions of no slip. In the frictional slip zones, $\tau_{rz}(r_1,z) = \mu\sigma_{rr}(r_1,z)$ and there can be slip ($[W] \neq 0$). In regions where there is no slip, the interface acts like a perfect interface ($[U] = [W] = 0$) and all that is known about the shear stress is that it is less than $\mu\sigma_{rr}(r_1,z)$. The interfacial shear stress must be determined by the stress analysis. A complicating feature of correctly modeling friction is that the sizes of the slip and contact zones are part of the problem and cannot be specified in the boundary conditions. Numerous authors have modeled friction by adding a constant "frictional" stress boundary condition to the interface. This approach may give qualitative information about the effect of friction, but it is not a correct model for a debonded interface with friction.

For stress analysis of the fragmentation specimen, we introduce a dimensionless coordinate system by normalizing positions and displacements to the fiber radius

$$\xi = \frac{r}{r_1}, \quad \zeta = \frac{z}{r_1}, \quad w_i = \frac{W_i}{r_1}, \quad \text{and} \quad u_i = \frac{U_i}{r_1} \tag{11}$$

In the dimensionless coordinates, the fiber extends from $\zeta = -\rho$ to $+\rho$ where

$$\rho = \frac{l}{2r_1}, \tag{12}$$

is the aspect ratio of the fragment. Finally, when using Hashin's imperfect interface model we use

$$[w] = \frac{\tau_{rz}(1,\zeta)}{d_s}, \tag{13}$$

where the new interface parameter, has units of stress and is given by $d_s = r_1 D_s$.

We split the stress analysis problem with arbitrary interface conditions into far-field stresses and perturbation stresses. By superposition, we write the *exact* solution to the fragmentation stress problem as

$$\begin{aligned} \sigma_{ij} &= \sigma_{ij}^{(\infty)} + \psi_\infty \sigma_{ij}^{(p)}, & \varepsilon_{ij} &= \varepsilon_{ij}^{(\infty)} + \psi_\infty \varepsilon_{ij}^{(p)}, \\ u_i &= u_i^{(\infty)} + \psi_\infty u_i^{(p)}, & w_i &= w_i^{(\infty)} + \psi_\infty w_i^{(p)}. \end{aligned} \tag{14}$$

The superscript $(\infty)$ indicates solution to the far-field stresses or the stresses for an infinite, unbroken fiber perfectly bonded to an infinite matrix. As shown in [7] the far-field stresses are:

$$\begin{aligned} &\sigma_{zz,1} = \psi_\infty, \quad \sigma_{rr,1} = \sigma_\infty, \quad \sigma_{\theta\theta,1} = \sigma_\infty, \quad \tau_{rz,1} = 0, \\ &\sigma_{zz,2} = \sigma_0, \quad \sigma_{rr,2} = \frac{\sigma_\infty}{\xi^2}, \quad \sigma_{\theta\theta,2} = -\frac{\sigma_\infty}{\xi^2}, \quad \tau_{rz,2} = 0, \end{aligned} \tag{15}$$

where $\psi_\infty$ and $\sigma_\infty$ are

$$\begin{aligned} \psi_\infty &= \frac{1}{\dfrac{2\nu_A^2}{E_A} - \dfrac{1-\nu_T}{E_T} - \dfrac{1+\nu_m}{E_m}} \\ &\quad \times \left[ \left( \frac{2\nu_A\nu_m}{E_A} - \frac{1-\nu_T}{E_T} - \frac{1+\nu_m}{E_m} \right) \frac{E_A\sigma_0}{E_m} \right. \\ &\quad \left. + \left( \frac{2\nu_A}{E_A}(\alpha_T - \alpha_m) + \left( \frac{1-\nu_T}{E_T} + \frac{1+\nu_m}{E_m} \right)(\alpha_A - \alpha_m) \right) E_A T \right], \end{aligned} \tag{16}$$

$$\sigma_\infty = \frac{-(\nu_A - \nu_m)\dfrac{\sigma_0}{E_m} + \big(\nu_A(\alpha_A - \alpha_m) + (\alpha_T - \alpha_m)\big)T}{\dfrac{2\nu_A^2}{E_A} - \dfrac{1-\nu_T}{E_T} - \dfrac{1+\nu_m}{E_m}}. \tag{17}$$

The anisotropic fiber is assumed to be transversely isotropic with the axial direction of symmetry coinciding with the axis of the fiber. The terms $E_A$, $E_T$, $\nu_A$, $\nu_T$, $\alpha_A$, and $\alpha_T$ are the axial and transverse moduli, Poisson's ratios, and thermal expansion coefficients of the fiber. The matrix is assumed to be isotropic. The terms $E_m$, $\nu_m$, and $\alpha_m$ are the modulus, Poisson's ratio, and thermal expansion coefficient of the matrix.

The superscript $(p)$ indicates the perturbation stresses. The perturbation stresses have been scaled by the far-field axial stress, $\psi_\infty$, in the fiber. The boundary conditions for the perturbation stresses are:

$$\begin{aligned} &\sigma_{zz,1}^{(p)}(r, z = \pm l/2) = -1, \qquad \tau_{rz,1}^{(p)}(r, z = \pm l/2) = \tau_{rz,2}^{(p)}(r, z = \pm l/2) = 0, \\ &w_2^{(p)}(r, z = \pm l/2) = 0. \end{aligned} \tag{18}$$

There is unit compression on the fiber ends and zero displacement on the matrix ends. Because the temperature differential was already included in the far-field stresses, $T = 0$ for the perturbation stresses. Because the far-field stresses are for a perfect interface, the interface conditions given above for an imperfect interface or a debonded interface are the interface conditions for the perturbation stresses alone. The only exception is when the interface conditions depend on the magnitude of the radial stresses. These conditions must use the total radial stress.

By using virtual work and the divergence theorem, it is possible to show that the total strain energy in the fiber and matrix for $\zeta$ between $-\rho$ to $+\rho$ is [7]:

$$\begin{aligned} U(\rho) &= \rho U_0 + \pi r_1^3 \psi_\infty^2 \left[ \int_0^1 2w_1^{(p)}(\xi, \rho)\xi d\xi \right. \\ &\quad \left. - \int_{-\rho}^{\rho} \left( \tau_{rz,2}^{(p)}(1, \zeta)[w^{(p)}] + \sigma_{rr,2}^{(p)}(1, \zeta)[u^{(p)}] \right) d\zeta \right], \end{aligned} \tag{19}$$

where $U_0$ is an infinite, but constant, term that includes the energy of the far-field stresses. In all interface conditions, we find that $\sigma_{rr,2}^{(p)}(1, \zeta)[u^{(p)}] = 0$. Thus the total energy reduces to

$$U(\rho) = \rho U_0 + \pi r_1^3 \psi_\infty^2 \left[ \int_0^1 2w_1^{(p)}(\rho)\xi d\xi - \int_{-\rho}^{\rho} \tau_{rz,2}^{(p)}(1, \zeta)[w^{(p)}] d\zeta \right]. \tag{20}$$

This equation is an *exact* expression of strain energy in a fiber/matrix fragment. The first integral is a crack closure integral over the fiber fracture surface. The crack-opening displacement ($\psi_\infty r_1 w_1(\rho)$) is multiplied by the crack-closure force ($2\pi r \psi_\infty dr$) and integrated over the fracture surface. The second integral is a closure integral for the imperfect or debonded interface. If the interface is perfect, this term is ignored. Because an imperfect or debonded interface allows the system to slip the total energy is reduced by an imperfect or debonded interface.

We next explicitly consider debond zones at each end of the fragment of dimensionless lengths $\delta_1$ and $\delta_2$. Formally, equation (20) still applies, but we should account for the possibility of unequal debond zones and the resulting asymmetry about $\zeta = 0$. The total energy becomes

$$\begin{aligned} U(\rho,\delta) &= \rho U_0 + \pi r_1^3 \psi_\infty^2 \left\{ \int_0^1 \left[ w_1^{(p)}(\xi,\rho) - w_1^{(p)}(\xi,-\rho) \right] \xi d\xi \right. \\ &\quad - \int_{-\rho}^{-(\rho-\delta_1)} \tau_{rz,2}^{(p)}(1,\zeta)[w^{(p)}]d\zeta \\ &\quad \left. - \int_{-(\rho-\delta_1)}^{(\rho-\delta_2)} \frac{{\tau_{rz,2}^{(p)}}^2(1,\zeta)}{d_s} d\zeta - \int_{\rho-\delta_2}^{\rho} \tau_{rz,2}^{(p)}(1,\zeta)[w^{(p)}]d\zeta \right\}, \end{aligned} \tag{21}$$

where $\delta = (\delta_1 + \delta_2)/2$ is the average debond length (many results in this paper will depend only on $\delta$ and not on the specific values of $\delta_1$ and $\delta_2$). We have accounted for unequal debond sizes by including fiber displacements at both ends of the fragment. We have further split the interfacial shear stress term into integrals over the two debond zones and the central intact zone. Finally, for the central intact zone we have used Hashin's imperfect interface model to eliminate $[w^{(p)}]$. To find the strain energy we need to find the fiber end displacements, the interfacial shear stress and displacement discontinuity in the debond zones, and the interfacial shear stress in the central intact, albeit perhaps imperfectly bonded, central zone.

When the fiber fractures during a fragmentation test, energy is released. Assuming that the fiber fracture occurs in the middle of a fragment of aspect ratio $\rho$ with average debond length $\delta$ resulting in two fragments of aspect ratio $\rho/2$ and average debond lengths $\delta/2$, the fiber fracture energy release rate is

$$G_f(\rho,\delta) = \frac{U(\rho,\delta) - 2U(\rho/2,\delta/2)}{\pi r_1^2}. \tag{22}$$

This energy release rate includes only the change in internal strain energy because the infinite matrix prevents any contribution from external work. Energy is also released by debond growth. If the average debond size increases by $d\delta$, the total debond area increases by $4\pi r_1^2 d\delta$; thus the energy release rate for debond growth is

$$G_d(\rho,\delta) = -\frac{1}{4\pi r_1^2} \frac{\partial U(\rho,\delta)}{\partial \delta}. \tag{23}$$

If the energy released by fiber fracture exceeds the energy required to fracture the fiber, the excess released energy may cause further damage to the fragmentation specimen. Some observed damage mechanisms are conical or straight cracks extending into the matrix [10, 11] and interfacial damage or debonding [12]. Here we will consider only the case where the excess released energy leads to interfacial damage or debonding. We begin with a fiber fragment of aspect ratio $\rho$ and initial average debond length of $\delta_i$. We assume the fiber fragments in the middle, and therefore splits into two fragments of aspect ratio $\rho/2$ and average debond lengths of $\delta_i/2$. If the fiber fracture event is followed by a simultaneous increase in average debond length to $\delta_f$, the total energy released due to fiber fracture and debonding is

$$\begin{aligned} -\Delta U(\rho,\delta^*) &= U(\rho,\delta_i) - 2U(\rho/2,\delta_f) \\ &= \pi r_1^2 G_f(\rho,\delta_i) + 8\pi r_1^2 \int_{\delta_i/2}^{\delta_f} G_d\left(\frac{\rho}{2},\delta\right) d\delta, \end{aligned} \tag{24}$$

where $\delta^* = 2(2\delta_f - \delta_i)$ is the *total* amount of simultaneous debonding.

## 3. APPROXIMATE THEORETICAL RESULTS

The results in the previous section are all exact provided we have an exact solution for the perturbation stresses. Unfortunately, no exact solution exists and we must therefore resort to using an approximate solution. We could use numerical solutions from finite element analyses, but the goal of this paper is to get analytical results. The most accurate solution for a fragmentation specimen with an imperfect interface is given in [7]. In brief, [7] presents a stress function solution based a Bessel-Fourier series. The solution exactly satisfies equilibrium and compatibility. It further satisfies most boundary conditions exactly. The single approximation is that the axial stress in the fiber at the fiber break is not exactly equal to zero, but rather only equal to zero when averaged over the fiber break surface. All the information from [7] required for the calculations in this paper are given in the Appendix.

First, consider a fragment with no debonds but possibly with an imperfect interface. From the Bessel-Fourier analysis [7], the fiber end displacement is

$$w_1^{(p)}(\xi,\rho) = \rho\frac{B_3(\rho)(1-\nu_T)}{2G_T}(\xi^2-1), \tag{25}$$

where $B_3(\rho)$ is the $B_3$ constant in the Bessel-Fourier analysis for a fragment of aspect ratio $\rho$. Making use of the imperfect interface condition $[w^{(p)}] = \tau_{rz,2}(1,\zeta)/d_s$ and doing the integrations in equation (20) we find

$$U(\rho,0) = \rho U_0 - \pi r_1^3\psi_\infty^2 F(\rho), \tag{26}$$

where

$$\begin{aligned} F(x) \;=\; & \frac{xB_3(x)(1-\nu_T)}{4G_T} \\ & + \frac{x}{d_s}\sum_{i=1}^{\infty}\Big[a_{0i}^2K_1^2(k_i) - 2a_{0i}a_{1i}\big(2(1-\nu_m)K_1^2(k_i) - k_iK_0(k_i)K_1(k_i)\big) \\ & + a_{1i}^2\big(2(1-\nu_m)K_1(k_i) - k_iK_0(k_i)\big)^2\Big], \end{aligned} \tag{27}$$

and the constants in the summation term ($a_{0i}$, $a_{1i}$, and $k_i$) are evaluated for a fragment of aspect ratio $x$.

We can immediately write the energy release rate for fiber fracture as

$$G_f(\rho,0) = r_1\psi_\infty^2\left[2F(\rho/2) - F(\rho)\right]. \tag{28}$$

To evaluate $G_f(\rho,0)$ we must evaluate $F(x)$ using the Bessel-Fourier series analysis given in the Appendix. The Bessel-Fourier solution is given in terms of an infinite series. For numerical calculations this series is truncated at some finite number of terms. To get convergence, we need to include terms with sufficiently high frequency ($k_i$) to be able to represent the stress state near the fiber break. Because $k_i = i\pi/\rho$, the number of terms required for convergence is proportional to $\rho$. We found the proportionality constant to be close to 1 and therefore convergence requires the use of roughly $\rho$ terms. Figure 2 plots $G_f$ as a function of fiber break density or crack density for an isotropic glass fibers in a polymer matrix for various values of $d_s$ (see Table 1 for a list of material properties used for the calculations in this paper). For all values of $d_s$, $G_f(\rho,0)$ is constant at low crack density and decreases at high crack density. The constant value at low crack density is the long-fragment limit where there are no interactions between fiber breaks. For this system, the long-fragment limit is for crack densities less than 0.5 mm$^{-1}$. The decrease at high crack densities is a consequence of interactions between fiber breaks. $G_f(\rho,0)$ is strongly influenced by $d_s$. When $d_s$ is low, the interface can slip after fiber fracture. At low crack density, this slip releases extra energy and causes $G_f(\rho,0)$ to be higher than when the interface is perfect. But, at high crack density, $G_f(\rho,0)$ is lower when $d_s$ is low because the available energy was already released by the slip at low crack density.

To analyze debond effects, we include debond zones on either end of the fragment of lengths $\delta_1$ and $\delta_2$ giving an average debond length of $\delta = (\delta_1+\delta_2)/2$. We thus split the fiber fragment into three zones. The two debond zones emanate from the two fiber breaks; the central zone has aspect ratio $\rho-\delta$. We assume that the central zone has an intact interface, but it may have an imperfect interface characterized by interface

**Table 1.**
Thermal and mechanical properties used for the fibers and matrices in the calculations in this paper. The epoxy properties are for the epoxy used in [17]. The polymer properties are for the UV-curable polymer used in [12].

| Property | T50 Carbon | Epoxy | E Glass | Polymer |
|---|---|---|---|---|
| Diameter ($2r_1$) ($\mu$m) | 7 | | 15 | |
| Tensile Modulus ($E_A$ or $E_m$) (GPa) | 390 | 2.6 | 72 | 1.68 |
| Transverse Modulus ($E_T$) (GPa) | 14 | | | |
| Axial Shear Modulus ($G_A$ or $G_m$) (GPa) | 20 | 0.97 | 30 | 0.62 |
| Axial Poisson's Ratio ($\nu_A$ or $\nu_m$) | 0.20 | 0.34 | 0.20 | 0.355 |
| Transverse Poisson's Ratio ($\nu_T$) | 0.25 | | | |
| Axial CTE ($\alpha_A$ or $\alpha_m$) ($10^{-6}$/°C) | -0.36 | 40 | 5.4 | 40 |
| Transverse CTE ($\alpha_T$) ($10^{-6}$/°C) | 18 | | | |

parameter $d_s$. The boundary conditions on the debond zones have the fragment end conditions on one end and continuity of displacements and stresses with the central zone on the other end. The interface conditions in the debond zone are the conditions for interfaces with or without friction. The interface conditions with friction are difficult to do correctly. For the purpose of illustrating energy methods, we will ignore friction effects. Some possible consequences of friction are covered in the discussion. We thus proceed with an analysis of a frictionless debond zone.

Stresses in a frictionless debond zone can be recovered from the Bessel-Fourier analysis by taking the limit as $d_s \to 0$. Because there is no shear stress at the interface, there is no stress transfer and the constants $c_{ji}$ and $B_3$ become zero. We cannot find $B_2$ from equation (A13) in the Appendix, because that expression came from an axial displacement relation [7] that is no longer relevant during friction slip. Because there is no stress transfer, however, the perturbation fiber axial stress remains constant at $-1$. From equation (A1) in the Appendix we find $B_2 = -1$. Equation (A14) in the Appendix can be used, because it was derived

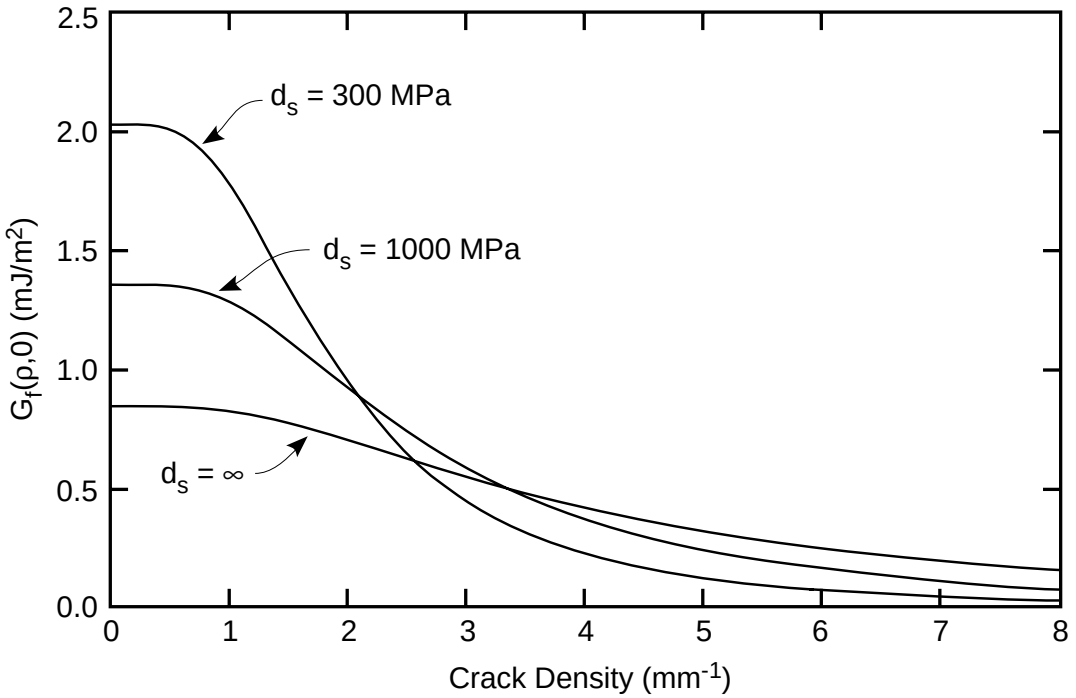


**Figure 2.** $G_f(\rho, 0)$ as a function of crack density for various values of $d_s$ using $\psi_\infty = 1$. The plot is for isotropic glass fibers in a polymer matrix.

from radial conditions [7]; it gives

$$B_1 = -\frac{\dfrac{\nu_A}{E_A}}{\dfrac{1+\nu_m}{E_m} + \dfrac{1-\nu_T}{E_T}}, \tag{29}$$

In summary, within frictionless debond zones the perturbation axial fiber stress is $-1$, there are no shear stresses, and the perturbation axial strain in the fiber, $\varepsilon_d^{(p)}$, is constant:

$$\varepsilon_d^{(p)} = -\frac{Q}{E_A}, \qquad \text{where} \qquad Q = 1 - \frac{\dfrac{2\nu_A^2}{E_A}}{\dfrac{1+\nu_m}{E_m} + \dfrac{1-\nu_T}{E_T}}. \tag{30}$$

This debond-zone result holds for both isotropic and anisotropic fibers.

For the central zone, we note that the shear stress and fiber axial stress end conditions are identical to the end conditions used when analyzing a fragment with no debonds. We thus will approximate the stresses in the central zone by the stresses in a fragment of axial ratio $\rho - \delta$ having no debonds. To find the the total energy in a fragment with debonds, we use equation (21) and write the displacement difference between the two fiber ends as the sum of the displacements across the debond zones and the central zone:

$$w_1^{(p)}(\xi,\rho) - w_1^{(p)}(\xi,-\rho) = -\frac{2\delta Q}{E_A} + 2w_1^{(p)}(\xi,\rho-\delta) \tag{31}$$

Combining this result with zero interfacial shear stress in the debond zones and the shear stress for a fragment of axial ratio $\rho - \delta$ in the central zone, the total energy is

$$U(\rho,\delta) = \rho U_0 - \pi r_1^3 \psi_\infty^2 \left[\frac{\delta Q}{E_A} + F(\rho-\delta)\right]. \tag{32}$$

The energy release rate for fiber fracture in the presence of debonds without any additional debonding is

$$G_f(\rho,\delta) = G_f(\rho-\delta,0). \tag{33}$$

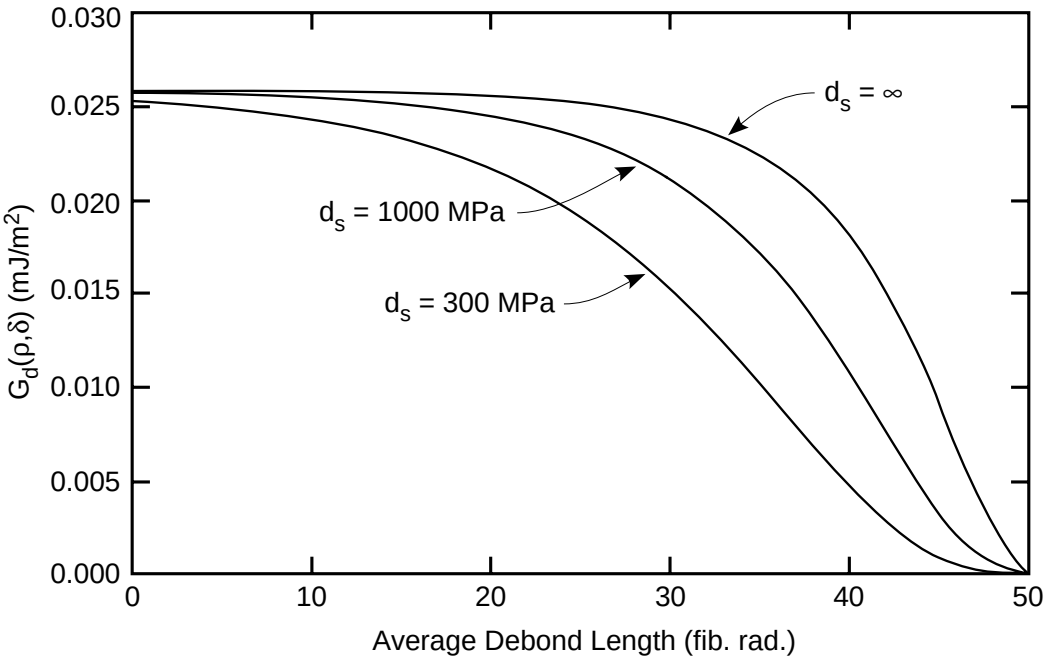


**Figure 3.** $G_d(\rho,\delta)$ as a function of debond length for various values of $d_s$ using $\psi_\infty = 1$. The plot is for isotropic glass fibers of aspect ratio $\rho = 50$ in a polymer matrix.

The energy release rate for debonding is

$$G_d(\rho,\delta) = \frac{r_1\psi_\infty^2}{4}\left[\frac{Q}{E_A} - F'(\rho-\delta)\right]. \tag{34}$$

Figure 3 plots $G_d(\rho,\delta)$ as a function of average debond length for an isotropic glass fiber of aspect ratio $\rho = 50$ in a polymer matrix for various values of $d_s$. All curves approach the same asymptotic limit for short debond lengths. As the debond grows, $G_d(\rho,\delta)$ drops, eventually reaching zero for complete debonding ($\delta = \rho$). $G_d(\rho,\delta)$ drops because the debond is encroaching on the neighboring fiber break and its debond. The drop is faster as $d_s$ gets lower. The asymptotic limit at short debond length is the long-fragment limit or the result when there are no interactions between neighboring fiber breaks. As stated previously, $G_f(\rho,0)$ has a long-fragment limit which occurs because $F(x)$ becomes constant for large $x$. We thus obtain a simple long-fragment limit for $G_d(\rho,\delta)$ of

$$\lim_{(\rho-\delta)\to\infty} G_d(\rho,\delta) = \frac{r_1\psi_\infty^2 Q}{4E_A}. \tag{35}$$

This limiting energy release rate is independent of both debond length and interface parameter $d_s$.

There is a new assumption in the debond analysis that was not present in the analysis without debonding. Although the shear stresses and fiber axial stresses are continuous at the junction between the debond zones and the central zone, the matrix tensile stress and radial displacements will not be continuous. As a consequence, this analysis ignores the details of the debond crack-tip stresses. For calculating energy release rates, we should consider the amount of energy released by the crack-tip stress. We claim that provided the debond crack tip is not too close to the fiber break that the crack tip stresses will remain unchanged as the debond propagates and therefore will release no energy. Some finite element calculations show that the debond crack-tip stresses are highly localized and release no energy for debond lengths greater than a few fiber diameters. For very short debond lengths, they do release energy and cause $G(\rho,\delta)$ to increase [13]. In summary, the $G_d(\rho,\delta)$ results here are accurate provided $\delta$ is greater than a few fiber diameters.

## 4. FRAGMENTATION WITH NO DEBONDING

The energy results derived in the previous section can be used as tools for analyzing fragmentation experiments. We begin by assuming that no debonding occurs during fragmentation. The implication is that the interface remains undamaged and that the fragmentation is purely a fiber failure test. The results, however, may be influenced by the ability of the intact interface to transfer stress which is characterized here by the interface parameter $d_s$. Although ignoring debonding is not a realistic model, we claim that the discrepancies between a zero-debonding analysis and experimental data are the information inherent in fragmentation experiments that might give information about interfacial failure.

We first attempt a fiber fragmentation prediction based on energy release rate for fiber fracture. It is now known that the density of microcracks in cross-ply laminates as a function of applied load can be predicted by assuming the next microcrack forms when the energy release rate for matrix cracking equals the matrix microcracking toughness [14–16]. For an analogous model of the fragmentation test, we assume the fiber fractures when $G_f(\rho,0) = G_{fc}$ where $G_{fc}$ is the fracture toughness of the fiber. Equating $G_{fc}$ to $G_f(\rho,0)$ and solving for $\psi_\infty$ gives

$$\psi_\infty = \sqrt{\frac{G_{fc}}{r_1\left[2F(\rho/2) - F(\rho)\right]}}. \tag{36}$$

Given $\psi_\infty$ and a level of thermal stresses, $T$, we can calculate applied strain as a function of $\rho$ or of crack density. Reversing this plot we predict crack density as a function of applied strain.

To judge the usefulness of the fiber-fracture energy model we compared predictions to experiments for T50 carbon fibers in an epoxy matrix [17]. From Raman experiments for stress transfer into similar carbon fibers [18], we can estimate that $d_s$ for these fibers is about 300 MPa [7]. The best fit to the fragmentation data using $d_s = 300$ MPa is given in Fig. 4; this fit required using $G_{fc} = 4600$ J/m$^2$. The prediction rises much more sharply than the experimental results. Although, this discrepancy could be corrected by allowing

the fiber toughness to depend on fragment length, there is a second problem which is more severe — the best fit $G_{fc}$ is unreasonably high. It is unlikely that T50 carbon fibers have a toughness in excess of 4000 J/m$^2$. In an attempt to improve the fit, we allowed $d_s$ to be an adjustable parameter. The resulting fit is better, but the initial rise is still too steep. Furthermore, the best fit parameters of $d_s = 40$ MPa and $G_{fc} = 10000$ J/m$^2$ are unrealistic — $d_s$ is too low to be consistent with Raman experiments [7, 18] and $G_{fc}$ is too high for brittle carbon fibers.

We conclude that fiber fracture in the fragmentation test is not controlled by the energy release rate for fiber fracture. We instead turn to the more conventional interpretation of fiber fragmentation whereby the fiber fragments when the stress in the fiber reaches the length-dependent strength of the fiber. Assuming the fiber fragments in the middle (the point of highest tensile stress), we need to solve $\langle \sigma_{zz,1}(l : \zeta = 0) \rangle = \sigma_{ult}(l)$ where $\langle \sigma_{zz,1}(l : \zeta = 0) \rangle$ is the average fiber stress in the middle of the fragment or length $l$ (or aspect ratio $l/2r_1$) and $\sigma_{ult}(l)$ is the length-dependent strength of the fibers. Proceeding as before we can solve for $\psi_\infty$ as a function of fragment length to get

$$\psi_\infty = \frac{\sigma_{ult}(l)}{1 + \left\langle \sigma^{(p)}_{zz,1}(l : \zeta = 0) \right\rangle}. \tag{37}$$

Given $\psi_\infty$ and a level of thermal stresses, $T$, we can calculate applied strain as a function of $l$ or of crack density $(1/l)$. Reversing this plot we get crack density as a function of applied strain. Any representation of fiber strength may be implemented in this analysis. The most common strength model is the two-parameter Weibull model, where the strength as a function of $l$ is

$$\sigma_{ult}(l) = \sigma_0 l^{-\frac{1}{\beta}} \Gamma\left(1 + \frac{1}{\beta}\right). \tag{38}$$

Here $\sigma_0$ and $\beta$ are the two Weibull parameters and $\Gamma(x)$ is the Gamma function. An alternate empirical approach is to fit experimental fiber strength results to a semi-log plot

$$\sigma_{ult}(l) = \beta_1 + \beta_2 \log l. \tag{39}$$

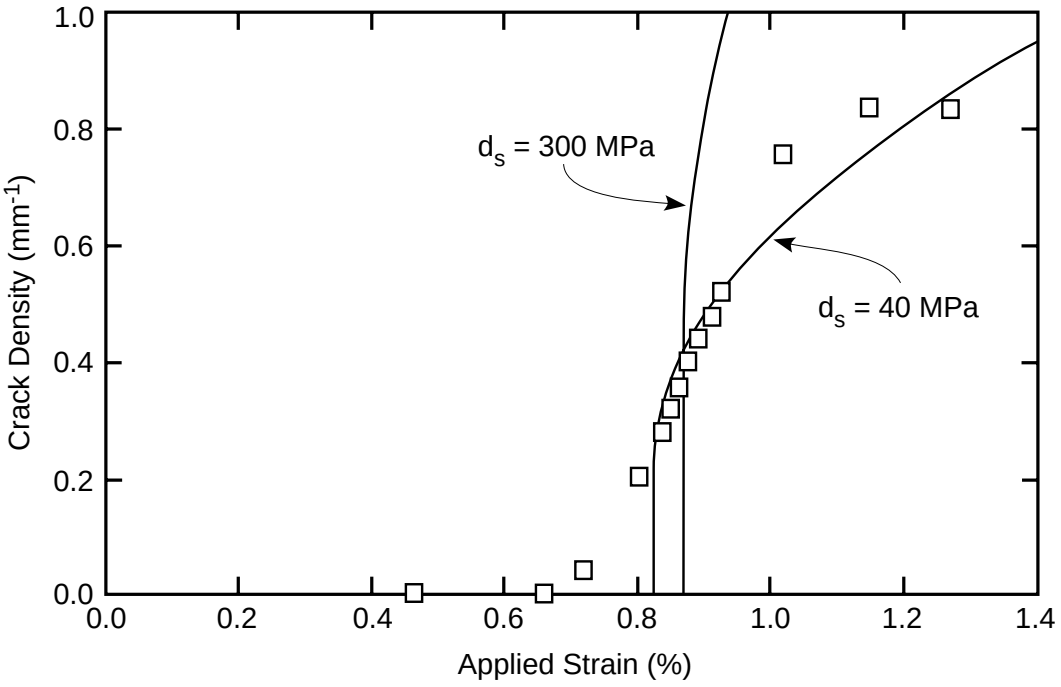


**Figure 4.** Predicted fragmentation results using a energy failure criterion for the fiber with no debonding compared to actual experiments. The two fits use $d_s = 300$ MPa and $G_{fc} = 4600$ J/m$^2$ or $d_s = 40$ MPa and $G_{fc} = 10000$ J/m$^2$. The experimental data are for T50 carbon fibers in an epoxy matrix.

Comparisons of the fiber strength model for various values of $d_s$ to experimental results are given in Fig. 5. For the fiber strength properties we used the experimental results given in [17]; they showed that fiber strength follows a semi-log relation with $\beta_1 = 3750$ MPa and $\beta_2 = 817$ MPa. The fits at low crack density are excellent and are independent of the interface parameter. The zero-debonding, fiber strength model is thus valid for low crack density. At higher crack density the experimental results plateau at a critical crack density. The perfect interface fit ($d_s = \infty$) never reaches a critical length. As $d_s$ gets lower, the prediction does bend over, but it never fits the experimental results.

## 5. FRAGMENTATION WITH DEBONDING

The fiber-strength model is a reasonable model for predicting fiber failures. Although fiber failure is not controlled by energy, $G_f(\rho, 0)$ is still a correct result for calculation of the amount of energy released when the fiber does break. During fragmentation of T50 carbon fibers, the energy released is large — 4600 to 10 000 J/m$^2$ depending on the value of $d_s$. Some of this energy will go into to fracturing the fiber, but the fracture of brittle carbon fibers probably requires very little energy. The remaining excess released energy may cause other damage in the specimen. Here we are considering debonding damage and thus consider modeling fragmentation when all the excess energy leads to growth of debonding

Consider an initial fragment of aspect ratio $\rho$ with average debond length of $\delta_i$. At some load this fragment breaks in the middle of the intact zone creating two fragments. We assume that the excess energy released by the fiber fracture causes debonding and therefore the average debond sizes in the two new fragments increase from $\delta_i/2$ to $\delta_f$; in other words there is a simultaneous average debond growth of $\delta_f - \delta_i/2$ in each fragment or a *total* amount of simultaneous debond growth of $\delta^* = 2(2\delta_f - \delta_i)$. The total energy released due to fiber fracture and debonding is

$$-\Delta U(\rho, \delta^*) = \pi r_1^2 G_f(\rho - \delta_i, 0) + 8\pi r_1^2 \int_{\delta_i/2}^{\delta_f} G_d\left(\frac{\rho}{2}, \delta\right) d\delta. \tag{40}$$

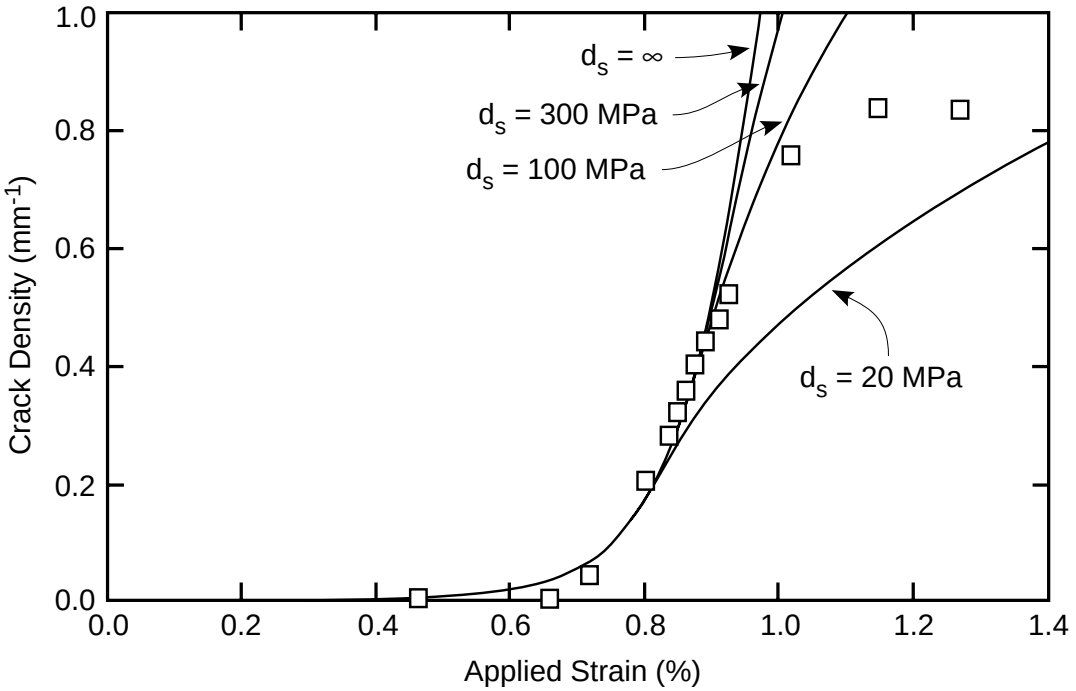


**Figure 5.** Predicted fragmentation results using a fiber strength model with no debonding for various values of $d_s$ compared to actual experiments. The experimental data are for T50 carbon fibers in an epoxy matrix.

Integrating $G_d(\rho/2, \delta)$ we find

$$\begin{aligned} -\Delta U(\rho, \delta^*) &= \pi r_1^2 G_f(\rho - \delta_i, 0) \\ &\quad + \pi r_1^3 \psi_\infty^2 \left[ \frac{\delta^* Q}{2E_A} + 2F\left( \frac{\rho - \delta_i}{2} - \frac{\delta^*}{4} \right) - 2F\left( \frac{\rho - \delta_i}{2} \right) \right]. \end{aligned} \tag{41}$$

Reference 12 proposed that the extent of simultaneous debonding can be predicted by equating the energy released by fiber fracture and debonding to the energy absorbed by the fracture surfaces. Thus, to predict $\delta^*$, we equate $-\Delta U(\rho, \delta^*)$ to

$$\text{Energy Absorbed} = \pi r_1^2 G_{fc} + 2\pi r_1^2 G_{dc} \delta^*, \tag{42}$$

where $G_{fc}$ is the fiber toughness and $G_{dc}$ is the interface toughness. The result, after partially solving for $\delta^*$, is

$$\delta^* = \frac{2E_A \left\{ G_f(\rho - \delta_i, 0) - G_{fc} + 2r_1 \psi_\infty^2 \left[ F\left( \frac{\rho - \delta_i}{2} - \frac{\delta^*}{4} \right) - F\left( \frac{\rho - \delta_i}{2} \right) \right] \right\}}{4E_A G_{dc} - r_1 \psi_\infty^2 Q}. \tag{43}$$

When analyzing fragmentation data, this equation must be solved numerically. The numerical process will only yield a solution if there is enough intact interface remaining to be able debond and absorb the energy released by the fiber. The maximum amount of interface that can debond is $\delta^* = 2(\rho - \delta_i)$. For a possibility of energy balance, we thus require

$$G_f(\rho - \delta_i, 0) - G_{fc} < 4G_{dc}(\rho - \delta_i) - r_1 \psi_\infty^2 \left[ \frac{(\rho - \delta_i)Q}{E_A} - 2F\left( \frac{\rho - \delta_i}{2} \right) \right], \tag{44}$$

where we have used the fact that $F(0) = 0$. If this inequality does not hold, the equation for $\delta^*$ cannot be solved. This condition physically corresponds to complete debonding after fiber fracture.

Equation (43) must be solved numerically because $\delta^*$ appears as an argument in $F(x)$. The situation simplifies in the long-fragment limit where $F(x)$ becomes constant. In the long-fragment limit, the analytical expression for $\delta^*$ is

$$\delta^* = \frac{2E_A \left( \lim_{\rho \to \infty} G_f(\rho, 0) - G_{fc} \right)}{4E_A G_{dc} - r_1 \psi_\infty^2 Q}. \tag{45}$$

This result is very similar to the analogous long-fragment result in [12], but there are several differences. First, equation (45) includes the effect of residual thermal stresses through terms in $\psi_\infty$. The result in [12] ignored residual thermal stresses and has fiber stress, $\sigma_f$ in place of $\psi_\infty$. The results in [12] can simply be corrected for residual stresses by replacing $\sigma_f$ by $\psi_\infty$. Second, the one-dimensional analysis in [12] had a long-fragment limit for $G_d(\rho, \delta)$ of

$$\lim_{(\rho - \delta) \to \infty} G_d(\rho, \delta) = \frac{r_1 \psi_\infty^2}{4} \frac{1}{E_A}, \tag{46}$$

which implies that $Q = 1$. This discrepancy is small because $Q \approx 1$ when the fiber modulus is much greater than the matrix modulus. The results in [12] can simply be corrected by including $Q$ in the debonding energy release rate term.

The third, and most significant, difference between equation (45) and [12] is the method for finding the long-fragment limit for $G_f(\rho, 0)$. Here we used the Bessel-Fourier series analysis and accounted for the possibility of an imperfect interface (using $d_s$). Reference 12 used a one-dimensional, shear-lag analysis and derived

$$\lim_{\rho - \infty} G_f(\rho, 0) = \frac{r_1 \psi_\infty^2}{E_f} \left( \frac{1}{\beta_{sl}} - \frac{\beta_{sl} E_f}{16 G_f} \right), \tag{47}$$

where

$$\beta_{sl} = \sqrt{\frac{2G_m}{E_f \ln\left( \frac{R}{r_1} \right)}} \tag{48}$$

is a "shear-lag" parameter. The parameter $\beta_{sl}$ depends on the radius $R$ of a fictitious stress concentration cylinder around the fiber. Because this radius is unknown, the shear-lag analysis gives an uncertain result. The new approach here has no unknown parameters and thus gives an explicit result for $\delta^*$ for a given value of $d_s$.

Figure 6 plots the long-fragment results for $\delta^*$ in equation (45) for various values of $d_s$ and for the shear lag result in [12]. The shear-lag plot used the recommended value $R/r_1 = 4$ [12]. The shear-lag result is effectively equivalent to the Bessel-Fourier analysis in this paper, but is offset from any particular $d_s$ result by the uncertainty in finding $\lim_{\rho-\infty} G_f(\rho, 0)$. This uncertainty is caused by the need to choose some value for $R/r_1$. The choice made in [12] was an excellent one for modeling a perfect interface. In principle, the results in this paper could be used to "calibrate" the shear-lag analysis by calculating the value of $R/r_1$ required to predict $\delta^*$ for any given value of $d_s$. An advantage of the new result in equation (45) is that no calibration is required.

We next consider modeling a complete fragment test using equation (43) rather then the long-fragment result in equation (45). The analysis begins by assuming an initial long fragment (such that all equations are in the long-fragment limit). Then, using the fiber strength failure model and equation (45), we can find $\psi_\infty$ (or equivalently applied strain) for the first fiber break and $\delta^*$ or the amount of debonding caused by the first fiber break. After the first fiber break, the average debond size becomes $\delta_i = \delta^*/4$. Once $\delta_i$ is known, we use the fiber strength model (equation (37)) to find $\psi_\infty$ for failure of a fragment of length $l = 2r_1(\rho - \delta_i)$ and equation (43) to find the amount of additional debonding. Finally, we use $\delta^*$ to find $\delta_f$ after the fiber break. This new value of $\delta_f$ becomes the input $\delta_i$ for finding the next fiber break. The end result is a calculation of both crack density and $\delta^*$ as a function of applied strain.

Comparisons of the fiber strength model with simultaneous debonding to experimental results are given in Fig. 5. The fit assumed a perfect interface ($d_s = \infty$) and assumed $G_{fc} = 10$ J/m$^2$ and $G_{dc} = 30.5$ J/m$^2$. The value of $G_{fc}$ is irrelevant as long as it is much less then the approximately 4000 J/m$^2$ released by fiber fracture events. The value of $G_{dc}$ has a much larger effect and can be varied to fit the high strain results. $G_{dc}$ is the only parameter in the analysis; thus by fitting fragmentation data we obtain an experimental result for interface toughness. The result for $G_{dc}$, however, depends on the value of $d_s$. As $d_s$ gets lower the

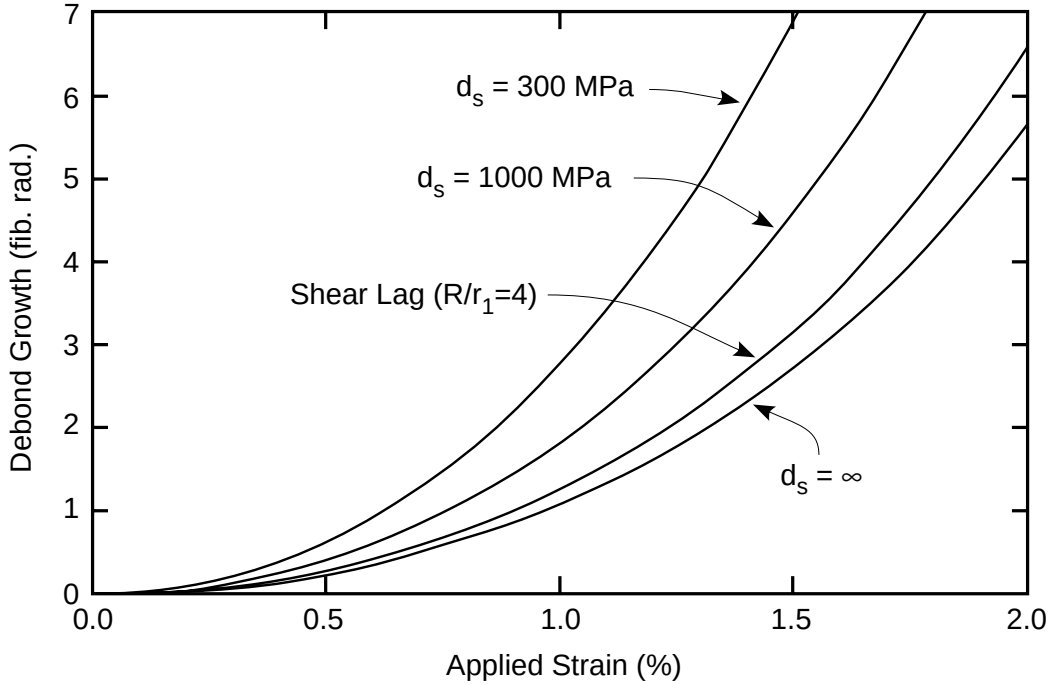


**Figure 6.** Long-fragment result for $\delta^*$ as a function of applied strain. The curves are for various values of $d_s$ and for the the analogous shear-lag predictions. This plot is for isotropic glass fibers in a polymer matrix and assumed that $G_{dc} = 200$ J/m$^2$.

value of $G_{dc}$ gets higher. Thus, to correctly determine $G_{dc}$, it is desirable to have a separate measurement of $d_s$ perhaps obtained by analysis of Raman experiments on stress transfer [7, 18].

The fact that we can fit fragmentation data is insufficient justification for the validity of the model. The model assumes a specific failure mechanism — that all the excess energy released by fiber fracture goes into causing debonding. If this failure mechanism is wrong, the model should not be used or should be modified to include a realistic failure mechanism. Thus all fragmentation models should be verified by experimental observations of interfacial failure mechanisms. For example, Fig. 7 also plots $\delta^*$ as a function of applied strain. The debonding predictions should be checked by comparing to debond observations; unfortunately, [17] did not report debonding results. Note that $\delta^*$ is the amount of debond growth occurring immediately after fiber fracture. If experimental observations of debonding measure average debond size over the entire specimen, then experiments should be compared to $\delta_i$ instead of $\delta^*$; $\delta_i$ can simply be calculated from $\delta^*$.

There are very few reports of measured debond lengths during fragmentation that can be used to test the debonding model. Wagner *et al.* [12] gives some partial results; they measured debond length as a function of applied strain at low crack density or in the long-fragment limit. We can compare their results to predictions using the long-fragment result in equation (45); a fit of Wagner's data [12] to equation (45) is given in Fig. 8. This fit used $d_s = \infty$ and $G_{dc} = 200$ J/m$^2$. Their is significant scatter in the data, but the fit can be used to derive an estimate for interfacial toughness. The $G_{dc}$ value here is slightly lower than the $G_{dc} = 264$ J/m$^2$ result in [12]. This discrepancy is caused by the different expressions used to find $\delta^*$. Both of these values are reasonable toughness values for an interface between glass fibers and a polymer matrix.

## 6. DISCUSSION

The goal of this paper was to investigate the use of fracture mechanics or energy methods for analyzing fragmentation experiments. All energy methods rely first on deriving an accurate stresses analysis for the fragmentation specimen and second on using that stress analysis to evaluate energy release rates for all relevant failure mechanisms. Here we considered only fiber fracture and debonding. We needed to calculate the axial stress in the fiber, the energy release rate for fiber fracture, and the energy release rate for interfacial

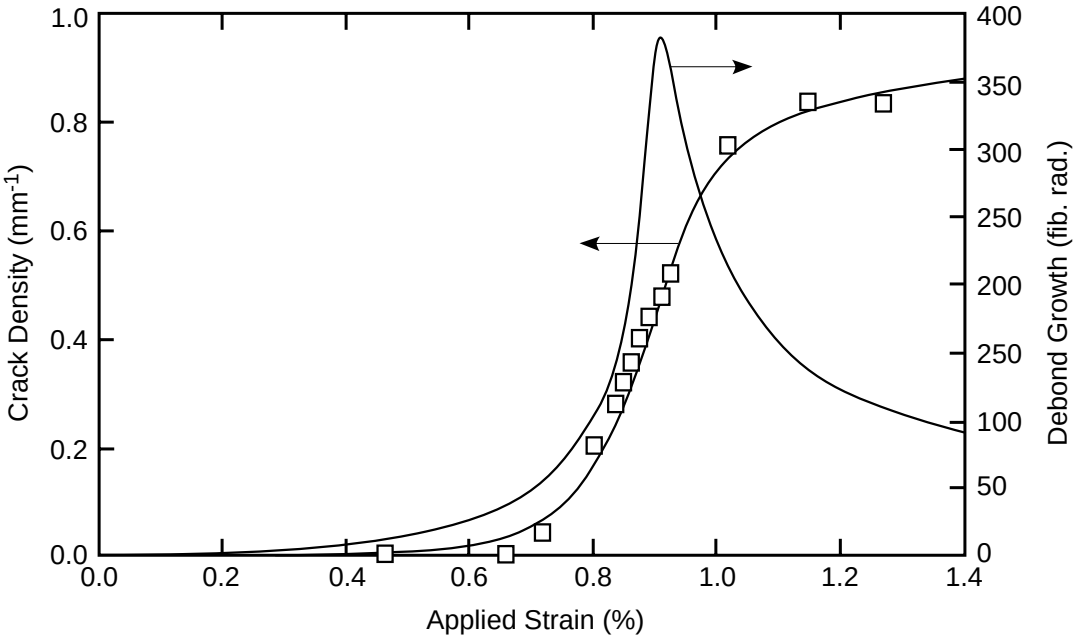


**Figure 7.** Predicted fragmentation and debond growth results using the fiber strength model with simultaneous debonding compared to actual experiments. The prediction assumed a perfect interface ($d_s = \infty$), a fiber toughness of $G_{fc} = 10$ J/m$^2$, and a debonding toughness of $G_{dc} = 30.5$ J/m$^2$. The experimental data is for T50 carbon fibers in an epoxy matrix.

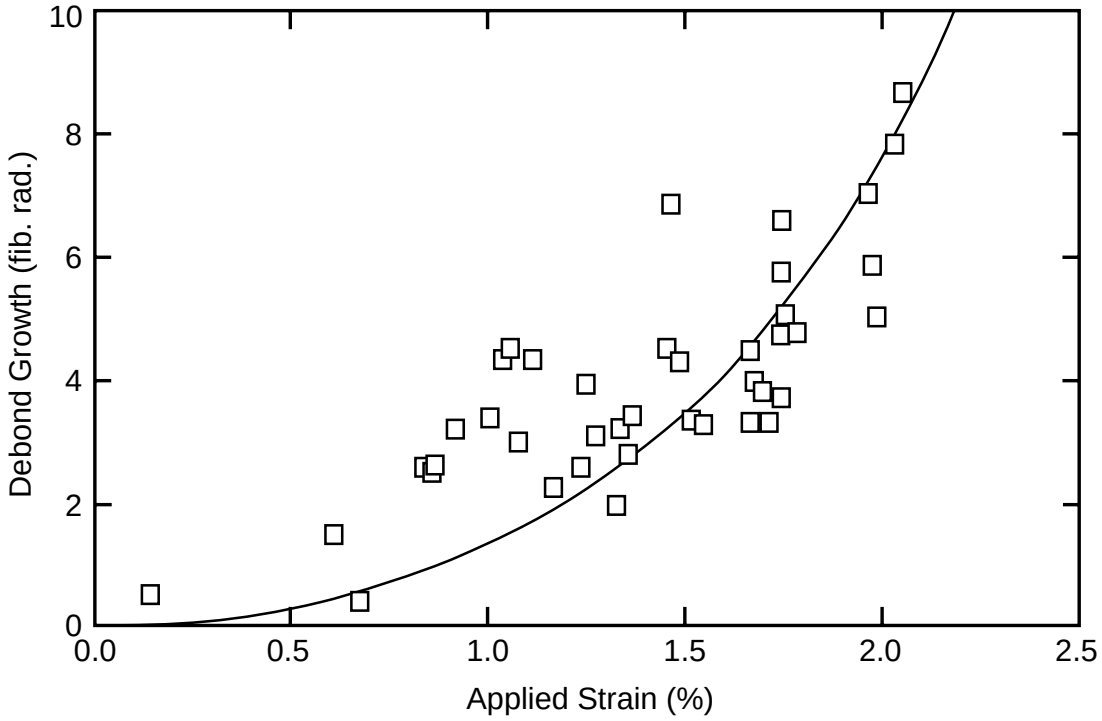


**Figure 8.** Long-fragment $\delta^*$ as a function of applied strain compared to experimental data. The fit curve used $d_s = \infty$ and $G_{dc} = 200$ J/m$^2$. The data is for E-glass fibers (with diameter $2r_1 = 18.4$ $\mu$m) in a polymer matrix.

debonding. All calculations were done using the Bessel-Fourier series analysis in [7]. In this section, we consider the accuracy of the required calculations.

First, fiber fracture is predicted to occur when the stress in the middle of a fragment of aspect ratio $\rho - \delta_i$ (the point of highest tensile stress) becomes equal to the strength of the fiber for that length or when

$$\psi_\infty \left(1 + \left\langle \sigma^{(p)}_{zz,1}(\rho - \delta_i : \zeta = 0)\right\rangle\right) = \sigma_{ult}(\rho - \delta_i). \tag{49}$$

Thus, predicting fiber fracture involves accurately determining the average perturbation axial stress in the middle of the fiber fragment. Now, recall that the Bessel-Fourier series method is an exact elasticity solution except for the axial stress end condition on the fiber. By Saint-Venant's principle, the stress solution is expected to be exact except for regions near the fiber break. Because $\langle \sigma^{(p)}_{zz,1}(\rho - \delta_i : \zeta = 0)\rangle$ is evaluated as far away from the break as possible, it is expected to be very accurate.

Calculating the amount of energy released by a fracturing fiber, $G_f(\rho - \delta_i, 0)$, is a much harder problem. The solution is equivalent to solving the fracture mechanics problem for a penny-shaped crack in a heterogeneous structure — a problem which has not yet been solved. In an attempt to judge the accuracy for $G_f(\rho - \delta_i, 0)$, we compared it to finite element analysis (FEA) calculations. The comparison, shown in Fig. 9, shows that the Bessel-Fourier result agrees with FEA results at high crack density, but is a factor of two higher than the FEA results at low crack density. The low crack density results are important because they include the long-fragment limit result for $G_f(\rho, 0)$. Unfortunately, it is not certain whether or not the FEA results are correct. The FEA calculation involves selecting a mesh around a crack tip at a bimaterial interface with two materials that differ significantly in their mechanical problems. The FEA results are mesh dependent; *i.e.*, they are not converged. As we continued to refine the mesh within the limits of computer memory and implemented crack-tip elements, the FEA result for $G_f(\rho, 0)$ continued to increase. We suggest that the correct result for $G_f(\rho, 0)$ lies between the Bessel-Fourier analysis and the FEA calculations.

Accurately calculating $G_f(\rho, \delta_i)$ remains an important problem for using energy methods to analyze fragmentation experiments. We have recently tried to refine the Bessel-Fourier series analysis [19]. In brief,

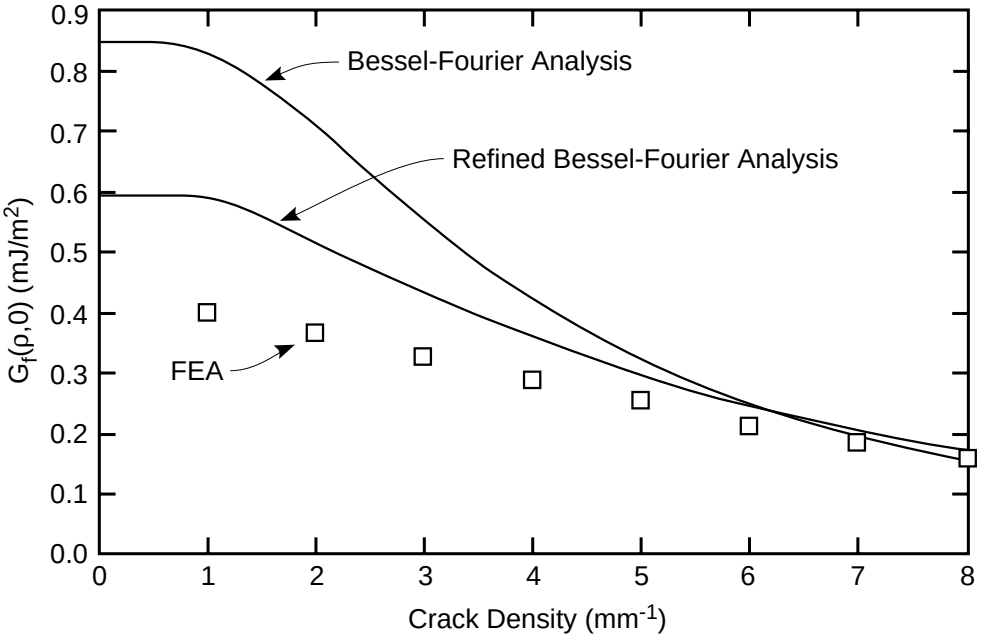


**Figure 9.** $G_f(\rho, 0)$ as a function of crack density using the Bessel-Fourier series analysis, an FEA analysis, or a refined Bessel-Fourier analysis. The plot is for isotropic glass fibers in a polymer matrix with a perfect interface ($d_s = \infty$) using $\psi_\infty = 1$.

we can add more terms to the fiber stress function that are consistent with all boundary conditions, but contribute non-zero axial stress on the fiber break surface. These extra terms allow us to compensate for the errors in the fiber end stress inherent in the initial Bessel-Fourier series [7]. With enough extra terms, the axial stress on the fiber break can be made arbitrarily close to zero (or $-1$ in the perturbation stresses). In theory, the refined calculation can therefore be made arbitrary close to the exact result. Figure 9 includes a plot of $G_f(\rho, 0)$ calculated using the refined Bessel-Fourier series analysis [19]. The results fall between the initial Bessel-Fourier analysis and the FEA results, but are still 50% higher than the FEA results at low crack density. We are currently exploring alternative techniques that can resolve the question about the correct result for fiber fracture energy release rate.

We used an very simple analysis to find the energy release rate for debonding, $G_d(\rho, \delta)$, for the case of a frictionless interface. Despite its simplicity, $G_d(\rho, \delta)$ is expected to very accurate except for very short debond lengths ($\delta$ less than a few fiber diameters). The concern about $G_d(\rho, \delta)$ is not its accuracy, but the effect of friction which is expected to present in real experiments. In the presence of friction, the interface will slip less than when it is frictionless. The consequence of less slippage is that $G_d(\rho, \delta)$ will be lower. The lowering effect will depend on the coefficient of friction.

When analyzing fragmentation experiments with simultaneous debonding, the extent of debonding can be estimated without any knowledge of $G_d(\rho, \delta)$. Revising the fiber-strength failure model to include a debond zone we can write

$$\psi_\infty = \frac{\sigma_{ult}(\rho - \delta_i)}{1 + \left\langle \sigma^{(p)}_{zz,1}(\rho - \delta_i : \zeta = 0) \right\rangle}. \tag{50}$$

Given experimental data for $\psi_\infty$ (calculated from applied strain and thermal load, $T$) and $\rho$ (calculated from crack density), we can solve equation (50) for debond size or $\delta_i$. In brief, the debond size can be back calculated from experimental data by looking at the difference between a zero-debonding analysis and the experimental results. This calculation will be inaccurate at low crack density, where the difference between experiments and zero-debonding predictions are small (see Fig. 5), but it will give a good estimate of $\delta_i$ at high crack density. The need for $G_d(\rho, \delta)$ arises when the goal is to deduce an interfacial toughness from experimental debond lengths. The results in Fig. 7 show that a frictionless analysis fits the results well and gives us one estimate of $G_{dc}$. Because there is no room for improvement, adding the effect of friction

cannot improve the model. What adding friction will do, however, is change the value of $G_{dc}$ required to fit experimental results. As the coefficient of friction increases, the apparent value of $G_{dc}$ will also increase. In summary, it will be a useful exercise to include friction in the analysis for $G_d(\rho, \delta)$. An accurate friction analysis, however, will provide no benefit in interpreting fragmentation results unless there are independent experimental results that provide the coefficient of friction.

A complete set of fragmentation experiments includes the fiber break or crack density as a function of applied strain. Modeling such experiments using energy methods requires input of fiber strength properties, the stress-transfer properties of the intact interface, $d_s$, the fiber toughness, the interfacial toughness, and the coefficient of friction for the interface. It appears impossible to deduce all require input properties by analysis of fragmentation results alone. Thus, fragmentation experiments should always be supplemented by other experiments. Fiber strength properties can be measured by experiments on isolated fibers. The interfacial stress-transfer properties can be measured using Raman spectroscopy [7, 18]. We need to develop methods for measuring the coefficient of friction. Given these input material properties, the fragmentation test provides the potential for measuring interfacial toughness, $G_{dc}$. Before a deduced $G_{dc}$ can be claimed to be an interfacial toughness, the model predictions must be compared to observations of debond sizes. If this comparison reveals errors, then the analysis will need to be modified to account for the actual failure mechanisms. Many other possible failure mechanisms will be amenable to the energy methods outlined in this paper.

*Acknowledgements*

This work was supported, in part, by a grant from the Mechanics of Materials program at NSF (CMS-9401772), and, in part, by a grant from the United States-Israel Binational Science Foundation (BSF Grant No. 92-00170), Jerusalem, Israel.

## REFERENCES

1. N. J. Wadsworth and I. Spilling, *Br. J. Appl. Phys. (J. Phys. D.)*, **1**, 1049–1058 (1968).
2. A. A. Fraser, F. H. Ancker and A. T. DiBenedetto, in: *Proc.* $30^{th}$ *Conf. SPI Reinforced Plastics Div.*, **Section 22-A**, pp. 1–13 (1975).
3. L. T. Drzal, M. J. Rich and P. F. Lloyd, *J. Adhesion*, **16**, 1–30 (1983).
4. W. D. Bascom and R. M.Jensen, *J. Adhesion*, **19**, 219–239 (1986).
5. W. D. Bascom, K-J. Yon, R. M. Jensen and L. Cordner, *J. Adhesion*, **34**, 79–98 (1991).
6. H. D. Wagner, H. E. Gallis and E. Wiesel, *J. Mat. Sci.*, **28**, 2238–2244 (1993).
7. J. A. Nairn and Y. C. Liu, *Int. J. Solids Structures*, **34**, 1255–1281 (1997).
8. Z. Hashin, *Mech. of Materials*, **8**, 333–348 (1990).
9. Z. Hashin, in: *Inelastic Deformation of Composite Materials*, G. J. Dvorak (Ed.), Springer-Verlag, New York, pp. 3–34 (1990).
10. P. Feillard, G. Désarmot and J. P. Favre, *Comp. Sci. Technol.*, **49**, 109–114 (1993).
11. P. Feillard, G. Désarmot and J. P. Favre, *Comp. Sci. Technol.*, **50**, 265–279 (1994).
12. H. D. Wagner, J. A. Nairn and M. Detassis, *Applied Comp. Mater.*, **2**, 107–117 (1995).
13. C. H. Liu and J. A. Nairn, Unpublished Results (1996).
14. J. A. Nairn, S. Hu and J. S. Bark, *J. Mat. Sci.*, **28**, 5099–5111 (1993).
15. J. A. Nairn and S. Hu, in: *Damage Mechanics of Composite Materials*, Ramesh Talreja (Ed.), Elsevier, Amsterdam, pp. 187–243 (1994).
16. J. A. Nairn, in: *Proc.* $10^{th}$ *Int'l Conf. on Comp. Mat.,* Whistler, British Columbia, Canada, **I**, pp. 423–430 (1995).
17. Y. Huang and R. J. Young, *Comp. Sci. Technol.*, **52**, 505–517 (1994).
18. N. Melanitis, C. Galiotis, P. L. Tetlow and C. K. L. Davies, *J. Mat. Sci.*, **28**, 1648–1654 (1993).
19. Y. C. Liu and J. A. Nairn, Unpublished Results (1996).
20. S. G. Lekhnitski, *Theory of an Anisotropic Body*. MIR Publishers, Moscow (1981).

## APPENDIX

In a recent paper [7], the stresses in a fiber fragment in a fragmentation specimen were analyzed using a Bessel-Fourier series stress function. The stress analysis satisfies equilibrium and compatibility exactly. It further satisfies all boundary conditions

exactly except for the perturbation axial stress on the fiber end. Instead of the perturbation fiber end stress being exactly -1, only the average perturbation fiber end stress is equal to -1. Substituting the stress function in [7] into the equations in [20] it is possible to find any component of stress, strain, or displacement. Here we quote only those results from [7] that are necessary for the calculations in this paper. The required results for a transversely isotropic fiber are

$$\left\langle \sigma_{zz,1}^{(p)} \right\rangle = B_2 + \frac{B_3 d}{2} + B_3 \sum_{i=1}^{\infty} \cos k_i\zeta \left[ c_{1i} \left( \frac{c}{s_1^2} - d \right) \frac{I_1(\beta_{1i})}{\beta_{1i}} + c_{2i} \left( \frac{c}{s_2^2} - d \right) \frac{I_1(\beta_{2i})}{\beta_{2i}} \right], \tag{A1}$$

$$\begin{aligned} w_1^{(p)} = {} & \zeta \left( \frac{B_2}{E_A} - \frac{2\nu_A B_1}{E_A} \right) + \frac{B_3}{2G_T} \left[ (1-\nu_T)\xi^2\zeta + \frac{2\nu_A E_T \rho^2}{3E_A}\zeta \right] \\ & + B_3 \sum_{i=1}^{\infty} \frac{\sin k_i\zeta}{k_i} \left[ (-1)^i \frac{8\nu_A(1+\nu_T)}{E_A k_i^2} + c_{1i} \left( \frac{1}{s_1^2 G_A} - \frac{d+2\nu_A a}{E_A} \right) I_0(\beta_{1i} r) \right. \\ & \left. + c_{2i} \left( \frac{1}{s_2^2 G_A} - \frac{d+2\nu_A a}{E_A} \right) I_0(\beta_{2i} r) \right], \end{aligned} \tag{A2}$$

$$\begin{aligned} \varepsilon_{zz,1}^{(p)} = \frac{\partial w_1}{\partial \zeta} = {} & -\frac{2\nu_A B_1}{E_A} + \frac{B_2}{E_A} + \frac{B_3}{2G_T} \left[ (1-\nu_T)\xi^2 + \frac{2\nu_A E_T \rho^2}{3E_A} \right] \\ & + B_3 \sum_{i=1}^{\infty} \cos k_i\zeta \left[ (-1)^i \frac{8\nu_A(1+\nu_T)}{E_A k_i^2} + c_{1i} \left( \frac{1}{s_1^2 G_A} - \frac{d+2\nu_A a}{E_A} \right) I_0(\beta_{1i}\xi) \right. \\ & \left. + c_{2i} \left( \frac{1}{s_2^2 G_A} - \frac{d+2\nu_A a}{E_A} \right) I_0(\beta_{2i}\xi) \right], \end{aligned} \tag{A3}$$

where $\left\langle \sigma_{zz,1}^{(p)} \right\rangle$ is the average fiber stress. The shear stress in the isotropic matrix is

$$\tau_{rz,2}^{(p)} = B_3 \sum_{i=1}^{\infty} \sin k_i\zeta \left[ c_{3i} \left( -K_1(k_i\xi) \right) + c_{4i} \Big( 2(1-\nu_m) K_1(k_i\xi) - k_i\xi K_0(k_i\xi) \Big) \right] \tag{A4}$$

Unfortunately, the stresses for an isotropic fiber are not a special case of the anisotropic fiber. The required results for an isotropic fiber are

$$\left\langle \sigma_{zz,1}^{(p)} \right\rangle = B_2 + \frac{B_3}{2} + 2B_3 \sum_{i=1}^{\infty} \cos k_i\zeta \left[ c_{1i} \frac{I_1(k_i)}{k_i} + c_{2i} \left( I_0(k_i) + 2(1-\nu_f) \frac{I_1(k_i)}{k_i} \right) \right], \tag{A5}$$

$$\begin{aligned} w_1^{(p)} = {} & \zeta \left( \frac{B_2}{E_f} - \frac{2\nu_f B_1}{E_f} \right) + \frac{B_3}{2G_f} \left[ (1-\nu_f)\xi^2\zeta + \frac{2\nu_f \rho^2}{3}\zeta \right] \\ & + \frac{B_3}{2G_f} \sum_{i=1}^{\infty} \frac{\sin k_i\zeta}{k_i} \left[ (-1)^i \frac{8\nu_f}{k_i^2} + c_{1i} I_0(k_i\xi) + c_{2i} \Big( k_i\xi I_1(k_i\xi) + 4(1-\nu_f) I_0(k_i\xi) \Big) \right], \end{aligned} \tag{A6}$$

$$\begin{aligned} \varepsilon_{zz,1}^{(p)} = {} & -\frac{2\nu_f B_1}{E_f} + \frac{B_2}{E_f} + \frac{B_3}{2G_f} \left[ (1-\nu_f)\xi^2 + \frac{2\nu_f \rho^2}{3} \right] \\ & + \frac{B_3}{2G_f} \sum_{i=1}^{\infty} \cos k_i\zeta \left[ (-1)^i \frac{8\nu_f}{k_i^2} + c_{1i} I_0(k_i\xi) + c_{2i} \Big( k_i\xi I_1(k_i\xi) + 4(1-\nu_f) I_0(k_i\xi) \Big) \right], \end{aligned} \tag{A7}$$

where $E_f$, $G_f$, and $\nu_f$ are the Young's and shear moduli and Poisson's ratio of the fiber. In the above equations, $I_0(x)$ and $I_1(x)$ are modified Bessel functions of the first kind, $K_0(x)$ and $K_1(x)$ are modified Bessel functions of the second kind,

$$k_i = \frac{2r_1 i\pi}{l} = \frac{i\pi}{\rho}, \qquad \text{and} \qquad \beta_{ji} = \frac{k_i}{s_j} \tag{A8}$$

where

$$s_1^2 = \frac{a + c + \sqrt{(a+c)^2 - 4d}}{2d}, \qquad s_2^2 = \frac{a + c - \sqrt{(a+c)^2 - 4d}}{2d} \tag{A9}$$

and

$$a = \frac{-\nu_A(1+\nu_T)}{1-\frac{\nu_A^2 E_T}{E_A}}, \quad b = \frac{\nu_T - \frac{\nu_A E_T}{E_A}\left(\frac{E_A}{G_A}-\nu_A\right)}{1-\frac{\nu_A^2 E_T}{E_A}},$$
$$c = \frac{\frac{E_A}{G_A}-\nu_A(1+\nu_T)}{1-\frac{\nu_A^2 E_T}{E_A}}, \qquad d = \frac{\frac{E_A}{2G_T}(1-\nu_T)}{1-\frac{\nu_A^2 E_T}{E_A}}. \tag{A10}$$

The remaining terms ($B_1$, $B_2$, $B_3$ and $c_{ji}$) are unknowns that must be determined from the boundary and interface conditions. For an anisotropic fiber imperfectly bonded to a matrix with an interface parameter, $d_s$, the $c_{ji}$ constants are found by solving a $4 \times 4$ linear system for each term in the Bessel-Fourier series. In matrix form, the linear systems are

$$\begin{pmatrix} \left(a-\frac{1}{s_1^2}\right)\frac{I_1(\beta_{1i})}{s_1} & \left(a-\frac{1}{s_2^2}\right)\frac{I_1(\beta_{2i})}{s_2} \\ \left(a-\frac{1}{s_1^2}\right)I_0(\beta_{1i}) + \frac{(1-b)}{s_1^2}\frac{I_1(\beta_{1i})}{\beta_{1i}} & \left(a-\frac{1}{s_2^2}\right)I_0(\beta_{2i}) + \frac{(1-b)}{s_2^2}\frac{I_1(\beta_{2i})}{\beta_{2i}} \\ \frac{(b-1)}{s_1^2}\frac{I_1(\beta_{1i})}{2G_T\beta_{1i}} & \frac{(b-1)}{s_2^2}\frac{I_1(\beta_{2i})}{2G_T\beta_{2i}} \\ -\left(\frac{1}{s_1^2 G_A}-\frac{d+2\nu_A a}{E_A}\right)I_0(\beta_{1i}) - \left(\frac{1}{s_1^2}-a\right)\frac{\beta_{1i}I_1(\beta_{1i})}{d_s} & -\left(\frac{1}{s_2^2 G_A}-\frac{d+2\nu_A a}{E_A}\right)I_0(\beta_{2i}) - \left(\frac{1}{s_2^2}-a\right)\frac{\beta_{2i}I_1(\beta_{2i})}{d_s} \end{pmatrix}$$

$$\begin{pmatrix} -K_1(k_i) & 2(1-\nu_m)K_1(k_i) - k_i K_0(k_i) \\ K_0(k_i) + \frac{K_1(k_i)}{k_i} & -(1-2\nu_m)K_0(k_i) + k_i K_1(k_i) \\ -\frac{K_1(k_i)}{2G_m k_i} & -\frac{K_0(k_i)}{2G_m} \\ \frac{K_0(k_i)}{2G_m} & \frac{1}{2G_m}\left(k_i K_1(k_i) - 4(1-\nu_m)K_0(k_i)\right) \end{pmatrix} \begin{pmatrix} c_{1i} \\ c_{2i} \\ c_{3i} \\ c_{4i} \end{pmatrix} = \begin{pmatrix} 0 \\ (-1)^i \frac{4(1+\nu_T)}{k_i^2} \\ (-1)^i \frac{4(1-\nu_T)}{2G_T k_i^2} \\ (-1)^i \frac{8\nu_A(1+\nu_T)}{E_A k_i^2} \end{pmatrix} \tag{A11}$$

Once the $c_{ji}$ are known, the remaining constants can be found using

$$B_3 = -\left\{ \frac{E_A(1-\nu_T)}{2\left(\frac{1-\nu_T}{E_T}+\frac{1+\nu_m}{E_m}-\frac{2\nu_A^2}{E_A}\right)}\left[\frac{\nu_A a}{E_A}\left(\frac{1+\nu_m}{E_m}-\frac{1+\nu_T}{E_T}\right) - \frac{1}{G_T}\left(\frac{1-\nu_T}{E_T}+\frac{1+\nu_m}{E_m}\right)\right] + \frac{d}{2} + \sum_{i=1}^{\infty} 2(-1)^{-i}\left[c_{1i}\left(\frac{c}{s_1^2}-d\right)\frac{I_1(\beta_{1i})}{\beta_{1i}} + c_{2i}\left(\frac{c}{s_2^2}-d\right)\frac{I_1(\beta_{2i})}{\beta_{2i}}\right]\right\}^{-1}, \tag{A12}$$

$$B_2 = \frac{E_A(1-\nu_T)}{2\left(\frac{1-\nu_T}{E_T}+\frac{1+\nu_m}{E_m}-\frac{2\nu_A^2}{E_A}\right)}\left[\frac{\nu_A a}{E_A}\left(\frac{1+\nu_m}{E_m}-\frac{1+\nu_T}{E_T}\right) - \frac{1}{G_T}\left(\frac{1-\nu_T}{E_T}+\frac{1+\nu_m}{E_m}\right)\right]B_3, \tag{A13}$$

$$B_1 = \frac{\frac{\nu_A}{E_A}}{\frac{1-\nu_T}{E_T}+\frac{1+\nu_m}{E_m}}B_2 + B_3\left[\frac{(1+\nu_T)\rho^2}{3} + \frac{(1-\nu_T)a}{8}\frac{\frac{1}{G_m}-\frac{1}{G_T}}{\frac{1-\nu_T}{E_T}+\frac{1+\nu_m}{E_m}}\right]. \tag{A14}$$

When the fibers are isotropic, the equations for $c_{ji}$ are

$$\begin{pmatrix} -I_1(k_i) & -2(1-\nu_f)I_1(k_i) - k_i I_0(k_i) & -K_1(k_i) & 2(1-\nu_m)K_1(k_i) - k_i K_0(k_i) \\ -I_0(k_i) + \frac{I_1(k_i)}{k_i} & -(1-2\nu_f)I_0(k_i) - k_i I_1(k_i) & K_0(k_i) + \frac{K_1(k_i)}{k_i} & -(1-2\nu_m)K_0(k_i) + k_i K_1(k_i) \\ -\frac{I_1(k_i)}{2G_f k_i} & -\frac{I_0(k_i)}{2G_f} & -\frac{K_1(k_i)}{2G_m k_i} & -\frac{K_0(k_i)}{2G_m} \\ -\left(\frac{I_0(k_i)}{2G_f} + \frac{k_i I_1(k_i)}{d_s}\right) & -\left(\frac{1}{2G_f} + \frac{2(1-\nu_f)}{d_s}\right) k_i I_1(k_i) - \left(\frac{2(1-\nu_f)}{G_f} + \frac{k_i^2}{d_s}\right) I_0(k_i) & \frac{K_0(k_i)}{2G_m} & \frac{1}{2G_m}\left(k_i K_1(k_i) - 4(1-\nu_m)K_0(k_i)\right) \end{pmatrix} \begin{pmatrix} c_{1i} \\ c_{2i} \\ c_{3i} \\ c_{4i} \end{pmatrix} = \begin{pmatrix} 0 \\ (-1)^i \frac{4(1+\nu_f)}{k_i^2} \\ (-1)^i \frac{2(1-\nu_f)}{G_f k_i^2} \\ (-1)^i \frac{4\nu_f}{G_f k_i^2} \end{pmatrix} \tag{A15}$$

and the remaining constants are given by

$$B_3 = -\left\{ \frac{\nu_f^2 \left(\frac{1}{G_m} - \frac{1}{G_f}\right)}{2\left(\frac{(1-2\nu_f)}{G_f} + \frac{1}{G_m}\right)} - \frac{1}{2} + \sum_{i=1}^{\infty} 2(-1)^{-i} \left[ c_{1i} \frac{I_1(k_i)}{k_i} + c_{2i} \left( I_0(k_i) + 2(1-\nu_f)\frac{I_1(k_i)}{k_i} \right) \right] \right\}^{-1}, \tag{A16}$$

$$B_2 = \left[ \frac{\nu_f^2 \left(\frac{1}{G_m} - \frac{1}{G_f}\right)}{2\left(\frac{(1-2\nu_f)}{G_f} + \frac{1}{G_m}\right)} - 1 \right] B_3, \tag{A17}$$

$$B_1 = \frac{\frac{\nu_f}{E_f}}{\frac{1-\nu_f}{E_f} + \frac{1+\nu_m}{E_m}} B_2 + B_3 \left[ \frac{(1+\nu_f)\rho^2}{3} - \frac{\nu_f}{8} \frac{\frac{1}{G_m} - \frac{1}{G_f}}{\frac{1-\nu_f}{E_f} + \frac{1+\nu_m}{E_m}} \right]. \tag{A18}$$